Particle dynamics and spatial e^-e^+ density structures at QED cascading in circularly polarized standing waves

A. V. Bashinov,[1,*] P. Kumar,[2] and A. V. Kim[1]

[1]*Institute of Applied Physics, Russian Academy of Sciences, 603950 Nizhny Novgorod, Russia*

[2]*Department of Physics, University of Lucknow, 226007 Lucknow, India*

(Received 8 October 2016; published 21 April 2017)

We present a comprehensive analysis of longitudinal particle drifting in a standing circularly polarized wave at extreme intensities when quantum radiation reaction (RR) effects should be accounted for. To get an insight into the physics of this phenomenon we made a comparative study considering the RR force in the Landau–Lifshitz or quantum-corrected form, including the case of photon emission stochasticity. Specific features of particle dynamics have a strong impact on spatial structures of the electron-positron (e^-e^+) density created in vacuum through quantum electrodynamic (QED) cascades in counterpropagating laser pulses. Three-dimensional particle-in-cell modeling accounting for QED effects confirms realization of different pair plasma structures.

DOI: 10.1103/PhysRevA.95.042127

I. INTRODUCTION

Development of ELI [1], Appolon 10 [2], XCELS [3], and other projects aimed at obtaining extreme laser fields stimulates fundamental and applied studies of the interaction of superintense laser radiation with matter. One of the features of this interaction is a decisive role of photon emission by electrons (positrons) and the corresponding radiation reaction effect. The electron motion changes drastically due to the impact of photon emission [4]. As a result, for example, there may occur counterintuitive effects in a linearly polarized field, such as anomalous radiative trapping in a standing wave [5] and radiative trapping in a traveling wave [6]. Moreover, not only changes in particle momentum but also the quantum (stochastic) nature of the photon emission play an important role [7–10]. Another important feature is also that emitted hard photons with energies above 1 MeV in an extreme laser field can create electron-positron pairs through multiphoton Breit–Wheeler processes [11,12]. Eventually, both the distribution function of particles and field distribution can be modified substantially due to avalanche-like electron-positron pair production (electromagnetic cascade) [13] and back reaction of the produced plasma [14].

For efficient emission of hard photons and their decay into e^-e^+ pairs the critical factor is a transverse field which a particle experiences in its rest frame. A simple case with a strong transverse field is a couple of counterpropagating laser pulses. Most theoretical studies of e^-e^+ generation were recently devoted to this case, which is also very instructive for understanding the main physical processes involved in such QED plasma behavior. Already in the first paper by Bell and Kirk [13] a prolific pair production at intensities of 10^{24} W/cm^2 for a 1 μm laser with circular polarization was shown. The case with circular polarization differs from that with linear polarization. On the one hand, the electric field in the antinode plane of a circularly polarized standing wave is a steadily rotating vector, whereas in the case of linear polarization the electric field is oscillating in time. This fact can lead to enhancement of electromagnetic cascade growth rate in the circular polarization case as compared to linear polarization [15]. Moreover, as opposed to circular polarization, linearly polarized focused laser beams allow studying direct Schwinger pair creation [16]. The fundamental reason of that is the possibility of fast pair escaping from the vicinity of the electric-field antinode in the latter case. On the other hand, in the case of linear polarization the particle escaping normal to the electric field from the high-field region can be suppressed by the anomalous radiative trapping (ART) mode [5], whereas in a circularly polarized standing wave particles are drifting from the antinode to the node of electric field, because they are initially sitting on the top of the hump of ponderomotive potential (antinode region). Thus, different particle motion and dynamics of cascade growth rate in the field with different polarization can lead to different pair plasma structures. Despite quite a number of investigations devoted to pair plasma structures in counterpropagating laser beams with circular and linear polarizations [15,17–24], a detailed analysis of structures in the field with different polarizations, intensities, and focusing parameters would be fundamentally important.

The goal of the present work is to study the types of spatial e^-e^+ density structures that can be realized in vacuum through QED cascades in counterpropagating laser pulses with circular polarization. We consider in detail particle drifting in an inhomogeneous field, especially longitudinal drifting as the most important process of particle escape for counterpropagating pulses when standing-wave configuration is formed. To get an insight into the physics we first present long-term density distributions, showing that with radiation reaction effects only the normal radiative trapping (NRT) regime [5,25] is realized, unlike the case of linear polarization when particles can be trapped in the ART regime. In NRT and ART regimes particles are attracted due to the RR effect to electric-field node or antinode regions of a standing wave, respectively. Since QED cascades are mainly generated in the high-field region, we once again consider particular trajectories in the electric-field antinode. We revisit the earlier works devoted to a stationary trajectory in a rotating electric field. This trajectory in the form of a circle has a long way of study. It was first considered in Refs. [26,27] taking

*Corresponding author: bashinov@appl.sci-nnov.ru

into account radiation losses. Based on particle motion, the authors of Ref. [26] made an attempt to derive dispersion relations in plasma with the inverse Faraday effect taken into account. Later the electron motion was investigated with allowance for the Lorentz–Abraham–Dirac (LAD) force [28]. A nonlinear Thomson scattering cross section was found for different limiting cases: the so-called radiation-dominated case when the RR force is comparable with the Lorentz force and quantum [29]. The stationary trajectory not only allows us to obtain exact expressions for the ponderomotive force and dielectric permittivity but also determines stationary nonlinear plasma-field structures, accounting for the LAD force [30]. The dispersion relation characteristics of stationary trajectory were modified considering quantum corrections to the Landau–Lifshitz (LL) force [19,31]. In our paper we will show how the stochastic nature of photon emission changes this trajectory. Moreover, the stochasticity generates a new effect of particle diffusion, resulting in an additional channel of particle escape. At the same time, the stochasticity slows down longitudinal escape from the electric-field antinode to the node [7] due to strong perturbation of particle motion.

It is also important that, at intensities approaching 10^{24} W/cm^2, electromagnetic cascades start to be generated along this trajectory [13]. Cascade growth rates were estimated with different accuracy in Refs. [17,32–34]. However, analysis of QED cascade development in an inhomogeneous field should include all particle channels of escape from the high-field region. This was done for some particular cases in Ref. [35] for the transverse drift and in Refs. [7,36] considering numerically longitudinal particle motion from the electric-field antinode to the node. We present a comprehensive analysis of particle drifting at extreme intensities from which quantitative dependencies of escape rates as a function of field amplitude are obtained. Comparison of the pair production growth rates and the main particle loss rate connected with the longitudinal drifting shows that three fundamental modes of QED cascades may be formed in a standing circularly polarized wave, giving rise to density distributions peaked at the antinode or node or in both regions. This conclusion is confirmed by particle-in-cell (PIC) simulations.

II. PARTICLE MOTION: LONG-TERM DISTRIBUTION

We first consider the long-term density distribution of electrons initially uniformly distributed in a plane standing circularly polarized wave, with the radiation reaction effect taken into account. Of course, this is a direct consequence of single-electron motions, but it allows us to understand the asymptotic behavior of a particle ensemble. Such a consideration allows us to introduce ART and NRT regimes in a standing linearly polarized wave [5].

Without loss of generality, assume that electric **E** and magnetic **B** fields may be written in the form

$$\mathbf{E} = \mathrm{Re}[a\cos(y)(\mathbf{z} - i\mathbf{x})e^{it}], \tag{1}$$

$$\mathbf{B} = \mathrm{Re}[a\sin(y)(\mathbf{z} - i\mathbf{x})e^{it}]. \tag{2}$$

The fields are normalized to $m\omega_l c/e$, where ω_l is the laser frequency, m and $-e$ are the mass and charge of the electron, c is the velocity of light, the y axis is perpendicular to **E**, **B**, and y and t are normalized to c/ω_l and $1/\omega_l$, respectively. The momentum is normalized to mc. The equations of motion make an autonomous system:

$$\frac{dp_\parallel}{dt} = \frac{ap_\perp \sin(y)\sin(\varphi)}{\gamma} - F_r p_\parallel, \tag{3}$$

$$\frac{dp_\perp}{dt} = -a\cos(y)\cos(\varphi) - \frac{ap_\parallel \sin(y)\sin(\varphi)}{\gamma} - F_r p_\perp, \tag{4}$$

$$\frac{d\varphi}{dt} = -1 + \frac{a}{p_\perp}\left[\cos(y)\sin(\varphi) - \frac{p_\parallel}{\gamma}\sin(y)\cos(\varphi)\right], \tag{5}$$

$$\frac{dy}{dt} = \frac{p_\parallel}{\gamma}, \tag{6}$$

where dimensionless variables are used, $p_\parallel$ is the electron momentum along the y axis, $p_\perp$ is the magnitude of momentum projection on the xz plane, φ is the angle between **E** and the momentum projection on the xz plane counterclockwise measured from **E**, and γ is electron Lorentz factor. Momentum projections on the x and z axes are $p_x = p_\perp \sin(t+\varphi)$ and $p_z = p_\perp \cos(t+\varphi)$, respectively. F_r is the factor of the radiation reaction force $\mathbf{F_{rr}}$, so that $\mathbf{F_{rr}} = -\mathbf{p}F_r$. F_r can be considered within the framework of different approaches:

(1) Without the radiation reaction force,

$$F_r = 0. \tag{7}$$

(2) The radiation reaction force in the form of the Landau–Lifshitz force (the main term proportional to γ^2 [37]):

$$F_r = 2\alpha\eta a^2[\cos^2(y) + p_\parallel^2 + p_\perp^2 \sin^2(\varphi)]/(3\gamma), \tag{8}$$

where α is the fine-structure constant, $\eta = \frac{\hbar\omega_l}{mc^2}$, and $\hbar$ is Planck's constant. We omit here introduction of LAD force because it was described many times in the previous works and gives the same results as the LL force, while both of them are valid in the range of field frequency and field strength parameters [38]. In the ultrarelativistic case, radiation power P is related to F_r by $P \approx F_r p^2/\gamma$ to an accuracy of $1/\gamma^2$. Following Ref. [39], we introduce the radiation reaction force with quantum corrections.

(3) The radiation reaction force taking into account quantum corrections,

$$F_r = \frac{\alpha}{3\sqrt{3}\pi\eta\gamma}\int_0^\infty u\frac{4u^2+5u+4}{(1+u)^4}K_{2/3}(2u/3\chi)du, \tag{9}$$

where $K_\nu(x)$ is the modified Bessel function of the second kind of order ν, and quantum parameter [40,41]

$$\chi = a\eta\sqrt{\cos^2(y) + p_\parallel^2 + p_\perp^2\sin^2(\varphi)}. \tag{10}$$

The approximation of Eq. (9) can be found in Sec. A.

One more way of describing radiation losses is to use the quasiclassical approach [39]. Particle motion between two acts of photon emission is described by equations without radiation reaction force $F_r = 0$, and at the instant of emission the particle momentum decreases proportionally to the emitted photon momentum. This approach is modeled within the framework of the Monte Carlo method [7,14,42]. In our article we use the method described in Ref. [10].

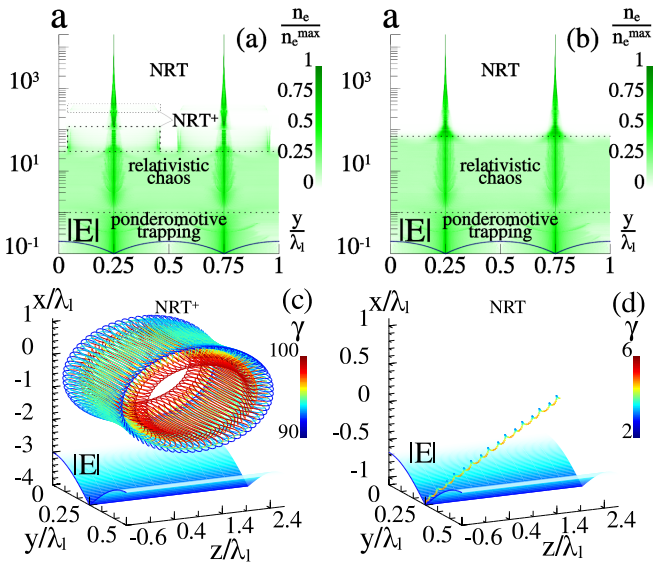

FIG. 1. Long-term electron-density distribution in the field of a plane circularly polarized standing wave as a function of wave amplitude in the frame of (a) approach (3) and (b) the quasiclassical approach. (c) NRT$^+$ and (d) NRT trajectories for wave amplitude $a = 100$. Color along the trajectory corresponds to the gamma factor. Surfaces under the trajectories represent $|\mathbf{E}|$.

Based on the introduced equations of motion it is possible to determine asymptotic regimes of motion in a circularly polarized field as was done in Ref. [5] in a linearly polarized field. The results are shown in Fig. 1. In the case of continuous force [Fig. 1(a)], Eq. (9) is used. Ponderomotive trapping, relativistic chaos, and NRT can be revealed as in the case of a linearly polarized field. Relativistic effects at $a \gtrsim 1$ lead to chaotization of motion. Particles do not accumulate at the electric-field node, they can randomly pass from one node to another. Radiation reaction effects become apparent at smaller wave amplitudes $a_{\mathrm{NRT}} \approx 30$ giving rise to the NRT regime (for a linearly polarized wave $a_{\mathrm{NRT}} \approx 400$). Although the radiation reaction force is much less than the Lorentz force at such amplitudes, over a long period of time the influence of dissipative force may be significant [4,25].

Along with the NRT trajectories there are special NRT$^+$ trajectories in the $30 < a < 120$; $280 < a < 390$ amplitude ranges. Unlike the NRT trajectories localized in a small region around the electric-field node, the amplitude of the oscillations along the y axis in the NRT$^+$ regime is $\Delta y \approx 0.4\lambda_l$, where λ_l is wavelength. On these trajectories the electron goes to the region of a strong electric field and is reflected from them about every field period. The average energy is $\gamma_{\mathrm{NRT}+} \approx a$, while in the NRT regime $\gamma_{\mathrm{NRT}} \ll a$. Moreover, as follows from numerical simulations, the NRT$^+$ trajectory is localized, whereas in the NRT regime the particle is drifting in the transverse plane xz with average velocity $0.6c$. The direction of drifting is determined by initial conditions. Examples of the trajectories are shown in Figs. 1(c) and 1(d).

There are also other special points of the system (3)–(6) $p_\parallel = 0$, $y = \lambda_l n/4$ ($n \in \mathbb{Z}$), $p_\perp = 0$. If a nonrelativistic electron appears in the vicinity of these points, it does not escape from this region [10]. It is kept there by the ponderomotive potential, which is in agreement with the vertical solid lines $y = \lambda_l/4$, $3\lambda_l/4$ in Fig. 1.

The use of the Landau–Lifshitz force does not lead to qualitative changes in Fig. 1(a). The only difference is a slight shift of the amplitude ranges of the NRT$^+$ regime to smaller amplitudes: $30 < a < 120$; $180 < a < 280$. Exclusion of radiation reaction stops the formation of the NRT regime, and there is only relativistic chaos at relativistic amplitudes. The stochasticity of photon emission, on the contrary, changes the motion regimes both quantitatively and qualitatively [Fig. 1(b)] in the frame of the quasiclassical approach. The NRT$^+$ regime does not arise, which testifies to the continuity and discreteness of radiation losses. The impact of photon emission on the electron does not allow the NRT$^+$ regime to emerge and the electron can skip to the region of other electric-field nodes, giving rise to relativistic chaos. Moreover, stochasticity of photon emission counteracts gradual cooling, which increases the threshold of the NRT regime $a_{\mathrm{NRT}} = 70$. It is interesting that there is no ART regime in a circularly polarized standing wave.

So, we have briefly described all stable asymptotic regimes, taking into account radiation losses. However, for fast processes like electron-positron pair production in extremely strong fields, the dynamic effects of motion can be very important. There is one more critical point at the electric-field antinode.

III. IMPACT OF RADIATION DISCRETENESS ON ELECTRON MOTION

It should be noted that the quantum-corrected RR force in Eqs. (3)–(6), used in most analytical treatments of ultrarelativistic particle dynamics, describes an average regular trajectory, while due to radiation discreteness actual motion changes randomly at the instant of emission. This may affect average particle characteristics, such as the mean relativistic factor (or mean energy) and rate of particle drifting. Such an impact was considered in Refs. [8–10] for a linearly polarized standing wave. In this section we address this issue to the circularly polarized wave, which, on the one hand, is a simpler field configuration but, on the other hand, a new effect of particle escape from a high-field region such as Brownian diffusion due to randomization of motion can also be generated.

Apparently Eqs. (3)–(6) admit stationary trajectories in the plane of the electric-field antinode. They were studied earlier in Refs. [19,26,27,30,31,38]. These trajectories are circles at the points $y = n\lambda_l/2$ and are governed by the following equations:

$$\begin{aligned} p_{\perp \mathrm{st}} &= a \sin(\varphi_{\mathrm{st}}), \\ a\cos(\varphi_{\mathrm{st}}) &= -F_{r\mathrm{st}} p_{\perp \mathrm{st}}, \\ p_{\parallel \mathrm{st}} &= 0, \\ \chi_{\mathrm{st}} &= \eta\sqrt{a^2 + p_{\perp \mathrm{st}}^4}, \\ \gamma_{\mathrm{st}} &= \sqrt{1 + p_{\perp \mathrm{st}}^2} = \sqrt{1 + \frac{a^2}{1 + F_{r\mathrm{st}}^2}}, \end{aligned} \tag{11}$$

where $F_{r\mathrm{st}}$ is defined by Eqs. (8) and (9) with all variables replaced by those with subindex st. Without radiation reaction we have $p_{\perp \mathrm{st}} = a$ and $\varphi_{\mathrm{st}} = \pi/2$. The angle between the electron momentum and the electric field φ_{st} becomes larger

than $\pi/2$ due to radiation reaction and the electric field performs positive work compensating radiative losses.

For further analytical consideration we need to specify asymptotic behavior of radiation reaction forces (8) and (9) in quantum and radiation-dominated regimes. The radiation-dominated regime occurs when $F_r \gg 0.2$, quantum effects become significant when $\chi \gg 0.2$. The threshold amplitudes of these regimes depend on wavelength [43]. Next, we focus on the optical frequency domain where the most powerful laser sources are expected. For the wavelength $\lambda_l = 0.8\ \mu$m, the thresholds of radiation-dominated and quantum regimes are approximately the same $a_{RR} \approx a_Q \approx 300$. When $a \gg a_Q, a_{RR}$, then the LL force (8) is $F_{rst} = 2\alpha\eta/3\gamma_{st}^3 \equiv \delta\gamma_{st}^3$ and the quantum-corrected force (9) is $F_{rst} = \frac{32\Gamma(2/3)}{3^{13/3}} \frac{\alpha\gamma_{st}^{1/3}}{\eta^{1/3}} \equiv \delta_q \gamma_{st}^{1/3}$. The validity condition of the LL force $a < 1/\eta$ ensures that $a < \gamma_{st}^2$. To generalize the expression for the gamma factor in the radiation-dominated or quantum regime we introduce

$$\gamma_{st} = \left(\frac{a}{\tilde{\delta}}\right)^{1-s}, \tag{12}$$

where for the LL or LAD forces $\tilde{\delta} = \delta$, $s = 3/4$ and for the quantum corrected force $\tilde{\delta} = \delta_q$, $s = 1/4$. Using this asymptotic behavior and assuming $a < 1/\eta$ we can simply find that $\gamma_{st}^2 > a$. The radiation reaction force and the quantum parameter are

$$F_{rst} = Da^s, \tag{13}$$

$$\chi_{st} = \eta D^{-2} a^{2(1-s)}, \tag{14}$$

where $D = \tilde{\delta}^{1-s}$. Without radiation reaction, $\gamma_{st} = a$ and $\chi_{st} = \eta a^2$. Thus, characteristics of the trajectories are very sensitive to the way we describe radiation losses. It is worth noting that, for the quantum-corrected RR force, Eqs. (12) and (14) approximate the gamma factor γ_{st}^{corr} and the quantum parameter χ_{st}^{corr} well at wave amplitudes $a \sim 100\,000$, while at reasonable values of a of the order of several thousands and $\lambda_l \approx 0.8\ \mu$m, a more suitable approximation is $\gamma_{st}^{corr} \approx 6.17 a^{0.695}$ and $\chi_{st}^{corr} \approx 1.8 \times 10^{-4} a^{1.34}$. The energy γ_{st}, quantum parameter χ_{st}, and angle ϕ_{st} characterizing stationary trajectories with different description of RR forces are compared in Fig. 2 (see also, e.g., Ref. [31]).

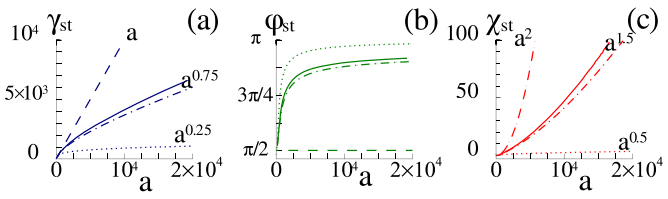

FIG. 2. (a) Lorentz factor, (b) angle between electric field and electron momentum, (c) quantum parameter χ_{st} at stationary trajectory as a function of the field amplitude of standing circularly polarized wave. The dash-dotted and dotted lines correspond to allowance for radiation reaction force with quantum corrections (9) and in accordance with Landau–Lifshitz form (8), respectively. Values obtained without radiation reaction are depicted by the dashed line. The solid line corresponds to quasiclassical case. Formulas show asymptotic behavior of trajectory parameters.

However, the quantum nature of photon emission is especially important at $\chi \gtrsim 1$: electrons randomly emit hard photons losing a significant part of their momentum and energy and after that they are accelerated fast again. In this case, due to random photon emission the particle motion is irregular, it rather has a fragmentary nature. Therefore, the averaged gamma factor as well as the quantum parameter do not need to have the same values as in the case with the quantum-corrected RR force. In the quasiclassical case, the particles have a possibility to gain energy up to a, while in the radiation-dominated regime the mean energy should be proportional to $a^{0.75}$, and the mean value of χ proportional to $a^{1.5}$ [34]. For determining the dependence of γ_{st}^Q, χ_{st}^Q, φ_{st}^Q on a for the case of interest we calculate the motion of 1000 particles at the antinode of electric field taking into account the stochasticity of emission. In the long-term evolution of such an ensemble, when the distribution function in momentum space is stabilized, we determine the corresponding mean values. So, according to the numerical simulations the gamma factor γ_{st}^Q and quantum parameter χ_{st}^Q are greater than the corresponding values of γ_{st}^{corr}, χ_{st}^{corr} in the case of quantum-corrected RR force, and the angle φ_{st}^Q is closer to π. These parameters as functions of a are varied as follows: $\gamma_{st}^Q = 1.13\gamma_{st}^{corr}$ and $\chi_{st}^Q = 1.15\chi_{st}^{corr}$. As we see, the stochasticity of photon emission just slightly corrects the mean values of χ and γ but, more importantly, it generates the new effect of particle diffusion mainly in the transverse directions. This occurs because each act of photon emission breaks the invariant $\mathbf{p}_\perp - \mathbf{A} = \mathbf{const}$., which causes additional drifting in the direction opposite to the photon momentum. Note that this diffusion exists even in a plane wave because it is connected with the stochastic nature of photon emission. A relativistic particle is shifted along a certain direction from its initial position after emission of n photons roughly at $\Delta = \sum_{i=0}^{n} \cos(\psi_i) c/W_\gamma$. ψ is the angle between the direction and drift velocity after photon emission, and W_γ is the probability of photon emission per unit time, $W_\gamma \approx \frac{1.46\alpha\omega_l\chi^{2/3}}{\eta\gamma}$ in the case of $\chi \gg 1$ [39]. ψ_i is uniformly distributed in the 0–2π range. Thus, the mean value is $\mu\Delta = 0$, dispersion is $\Theta\Delta = 0.5nc^2/W_\gamma^2$, and the diffusion coefficient is $d = 0.25c^2/W_\gamma$ or, in dimensionless variables,

$$d \approx \frac{\eta^{1/3}}{6\alpha\gamma_{st}^{Q\,1/3}}. \tag{15}$$

IV. LONGITUDINAL DRIFTING

As follows from the long-term density distributions shown in Fig. 1, the particles mainly tend to move from the high-electric-field (antinode) region to the minimum ponderomotive potential (node region). This is a quite expected result for a standing wave with circular polarization, although we note that the NRT$^+$ regime [Figs. 1(a) and 1(c)] with the classical description of the RR force and the ART regime in a linearly polarized standing wave [5] were unexpectedly new. However, for the problem of interest when pair plasma is generated primarily in the antinode region, it is important to know the rate of particle escape. To do so, we study the influence of radiation on the stability of the stationary trajectory given by Eqs. (11). Assuming $\mathbf{p} = \mathbf{p}_{st} + \tilde{\mathbf{p}}(t)$, $\varphi = \varphi_{st} + \tilde{\varphi}(t)$,

$y = y_{st} + \tilde{y}(t)$, where $\tilde{\mathbf{p}}(t)$, $\tilde{\varphi}(t)$, $\tilde{y}(t)$ are small perturbations, we substitute them into Eqs. (3)–(6). Then keeping only linear terms of the perturbations the governing equations are written as

$$\frac{d\tilde{p_\perp}}{dt} = p_{\perp st}\tilde{\varphi} - \tilde{F}_r p_{\perp st} - \tilde{p_\perp} F_{rst}, \tag{16}$$

$$\frac{d\tilde{\varphi}}{dt} = \frac{1}{p_{\perp st}}[-\tilde{p_\perp} + a\cos(\varphi_{st})\tilde{\varphi}], \tag{17}$$

$$\frac{d\tilde{p}_\parallel}{dt} = \frac{p_{\perp st}^2 \tilde{y}}{\gamma_{st}} - F_{rst}\tilde{p}_\parallel, \tag{18}$$

$$\frac{d\tilde{y}}{dt} = \frac{\tilde{p}_\parallel}{\gamma_{st}}. \tag{19}$$

Without loss of generality we assume $y_{st} = 0$. For comparative analysis we consider again different descriptions of radiation losses.

(1) LL force:

$$\tilde{F}_r = -\frac{2\alpha\eta}{3\gamma_{st}} a^2 p_{\perp st}^2 \sin(2\varphi_{st})\tilde{\varphi} + \frac{2\alpha\eta \tilde{p_\perp} p_{\perp st}}{3\gamma_{st}^3}\left(\gamma_{st}^4 - 1 - a^2\right). \tag{20}$$

(2) Quantum-corrected case:

$$\begin{aligned}\tilde{F}_r = {} & \frac{\alpha p_{\perp st}}{3\sqrt{3}\pi\eta\gamma_{st}}\left\{\frac{p_{\perp st}^2[\tilde{p_\perp} + a\cos(\varphi_{st})\tilde{\varphi}]}{3\chi_{st}(a^2 + p_{\perp st}^4)}\right. \\ & \times \int_0^\infty \frac{u^2(4u^2+5u+4)}{(1+u)^4} \\ & \times \left[K_{1/3}\left(\frac{2u}{3\chi_{st}}\right) + K_{5/3}\left(\frac{2u}{3\chi_{st}}\right)\right]du \\ & \left. - \frac{\tilde{p_\perp}}{\gamma_{st}^2}\int_0^\infty \frac{u(4u^2+5u+4)}{(1+u)^4} K_{2/3}\left(\frac{2u}{3\chi_{st}}\right)du\right\}. \end{aligned} \tag{21}$$

The system (16)–(19) can be divided into two pairs of equations (18), (19) and (16), (17). Solutions are written in the form $\tilde{p}_\parallel, \tilde{y} \propto e^{\lambda_\parallel t}$ and $\tilde{p_\perp}, \tilde{\varphi} \propto e^{\lambda_\perp t}$. Without radiation reaction $\lambda_{\parallel\pm} = \pm(\gamma^2 - 1)^{1/2}/\gamma$, in the ultrarelativistic case $\lambda_{\parallel\pm} = \pm 1$ and $\lambda_\perp = 0$. In a general case,

$$\lambda_{\parallel\pm} = 0.5\left(-F_{rst} \pm \sqrt{F_{rst}^2 + 4p_{\perp st}^2/\gamma_{st}^2}\right). \tag{22}$$

This means that $y = n\lambda_l/2$ is a saddle point, and the positive value corresponds to the rate of particle drifting along the y axis to the electric-field node. The asymptotic behavior of $\lambda_{\parallel\pm}$ for $a \gg a_{RR}$ is

$$\lambda_{\parallel -} \approx -F_r, \quad \lambda_{\parallel +} \approx 1/F_r. \tag{23}$$

In the case of LL force (as well as LAD force), $\lambda_{\parallel+}^{\mathrm{LL}} \propto a^{-0.75}$; for quantum-corrected force $\lambda_{\parallel+}^{\mathrm{corr}} \propto a^{-0.25}$. So, quantum corrections change not only the factor of power function, but also the power law and modify significantly the rate of longitudinal drifting. Note that, in the case of quantum-corrected force, $\lambda_{\parallel\pm}^{\mathrm{corr}}$ approaches the asymptotic behavior at $a \sim 100\,000$, whereas for the considered parameters $\lambda_{\parallel+}^{\mathrm{corr}} \approx 5.5a^{-0.3}$.

The two roots of $\lambda_\perp$ are complex conjugates having negative real parts. The stable focus is in the phase plane $\tilde{p_\perp}$, $\tilde{\phi}$. $\lambda_\parallel$ and $\lambda_\perp$ can be found numerically using Eqs. (16)–(19). $\lambda_{\parallel+}$, $\mathrm{Re}\lambda_\perp$ and their ratio are shown in Fig. 3.

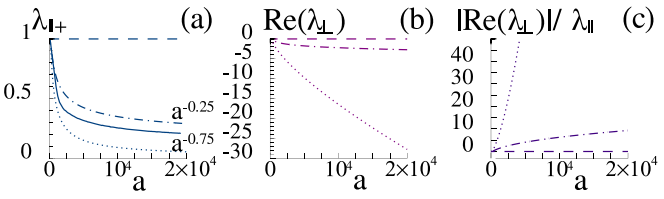

FIG. 3. (a) $\lambda_{\parallel+}$ escape rate of electrons along the y axis, (b) $\mathrm{Re}(\lambda_\perp)$ rate of approach to the stationary trajectory in transverse direction and (c) $|\mathrm{Re}(\lambda_\perp)|/\lambda_{\parallel+}$ ratio as a function of field amplitude of standing circularly polarized wave. Line style is the same as in Fig. 2.

First, the radiation reaction slows down the longitudinal drift and accelerates approach to the stationary trajectory in the transverse plane $(p_\perp, \phi)$. An ultrarelativistic particle radiates along its instant vector of velocity with angular spread $1/\gamma_e$ [44]. In the quantum case, when $\chi_e \gg 1$ angular distribution of radiated power can become larger $\sim \chi_e^{1/3}/\gamma_e$ [39]. However, even in the quantum case as follows from Eqs. (12) and (14) the angular spread $\sim(\alpha\eta/a)^{0.25} \approx 0.01a^{-0.25}$ is much less than unity, thus the photon emission counteracts motion in the direction of velocity. The stronger the radiation losses, the slower the longitudinal drift is. At the same time, in the transverse direction the particles tend to the stationary trajectory, where losses are compensated by positive work of the field. Second, when $a > 860$ in the case of classical approach with quantum corrections (in the case of LL force $a > 370$), we have the $|\mathrm{Re}(\lambda_\perp^{\mathrm{corr}})|/\lambda_{\parallel+}^{\mathrm{corr}} > 1$ ratio and the particles first quickly approach the stationary trajectory and after that slowly drift in the longitudinal direction to the electric-field node. So, the trajectory can be characterized by local values of the field, and inertia of particle motion can be neglected. Radiation reaction retards particles in the vicinity of the electric-field antinode, and the characteristic time of the drift from the electric-field antinode is $t_d \propto \lambda_{\parallel+}^{-1}$. The fact that t_d can be much longer than the optical cycle is explained not only by initial proximity to the electric-field antinode, but also by the small value of $\lambda_{\parallel+}$, which is important. In the case of using the LL (LAD) force, $\lambda_{\parallel+}$ and $\mathrm{Re}\lambda_\perp$ are underestimated at $a > a_Q$.

The qualitative behavior of $\lambda_{\parallel+}$ can be characterized by considering longitudinal motion in the radiation-dominated regime. In this regime $p_\parallel \ll p_\perp$, so the characteristics of the trajectory are determined by the local value of the field $a(y) = a\cos y$. Then the exact expression for ponderomotive force from Eqs. (3) and (11) is

$$F_p = -\frac{[a^2(y)]'}{2\gamma\left(1 + F_r^2\right)} = \frac{a^2\sin(2y)}{2\gamma\left(1 + F_r^2\right)}. \tag{24}$$

The same expression for ponderomotive force in the case of the LAD force has been obtained in Ref. [30]. Then assuming $\partial p_\parallel/\partial t \simeq 0$ in Eq. (3) we can obtain expressions for longitudinal momentum and velocity in the

radiation-dominated regime as long as $|\mathbf{E}(y)| \gg |\mathbf{B}(y)|$:

$$p_{\parallel} = \frac{F_p}{F_r} = \frac{\sin(2y)}{2D^2 a^{2s-1}\cos^{2s+1}(y)}, \tag{25}$$

$$v_{\parallel} = \frac{F_p}{\gamma F_r} = \frac{\sin(2y)}{2Da^s\cos^{2+s}(y)}. \tag{26}$$

The time of longitudinal drifting from the antinode of the electric field $t_d = \int dy/v_{\parallel}$, and $\lambda_{\parallel+} \propto a^{-s}$ is in agreement with Eq. (23).

To compare longitudinal drifting within the classical and quasiclassical approaches, we consider the evolution of $N_e = 1000$ electrons initially at rest located at the point $y = 0.001\lambda_l$ and determine the period of time t_n when the electrons' center of mass reaches the point $y = \lambda_l/4$. In the quasiclassical case, electron evolution is drift and diffusion. In the classical case, when $(\mathrm{Re}\lambda_{\perp})/\lambda_{\parallel+} > 1$, it follows from the linearized system of equations (16)–(19) that the trajectory in the vicinity of the electric-field antinode $y \ll \lambda_l/4$ [$\cos(y) \approx 1$] can be described by the expression

$$y = \frac{y_0}{\lambda_{\parallel-} - \lambda_{\parallel+}}(\lambda_{\parallel-}e^{\lambda_{\parallel+}t} - \lambda_{\parallel+}e^{\lambda_{\parallel-}t}), \tag{27}$$

and in the amplitude range $a \gg a_{RR}$,

$$y \approx y_0 e^{\lambda_{\parallel+}t}. \tag{28}$$

For small amplitudes $a < a_{RR}$ the influence of radiation losses over a short period of time is weak. Figure 4(a) corresponds to $a = 100$. The trajectories obtained with and without radiation reaction are approximately the same as long as the particles do not reach the region of strong magnetic field. After that, diffusion due to stochasticity of photon emission smooths the electron distribution. The upper boundary of electron distribution corresponds to the electrons that do not have enough time to emit a photon [dashed line in Fig. 4(a)]. Motion of the electrons' center of mass can be described within the framework of the classical approaches to radiation reaction description [solid, dotted, and dash-dotted lines in Fig. 4(a)]. However, the trajectory considered above under certain initial conditions does not approach the described stationary trajectory [the line marked by triangles differs from, for example, the dotted line in Fig. 4(a)]. In this case a dynamical stop effect occurs at $y \approx 0.1\lambda_l$. Radiation losses smooth this effect; for the same reason the slowest motion occurs without photon emission. Particles are not trapped at the closest node region.

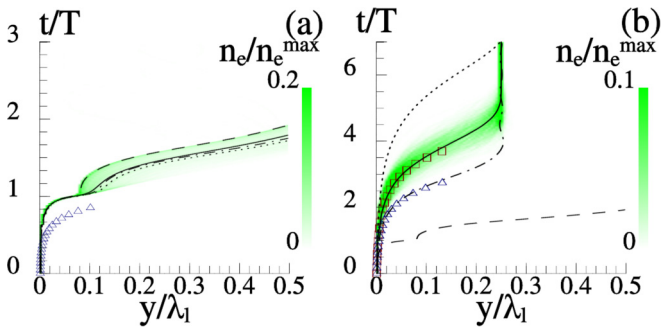

FIG. 4. Electron distribution evolution along y axis for wave amplitude (a) $a = 100$, and (b) $a = 20\,000$ in the quasiclassical case. Solid line corresponds to trajectory of mass center. Trajectories represented by dashed and dotted lines were obtained without and with radiation reaction in Landau–Lifshitz form, respectively. Quantum corrections to Landau–Lifshitz force give the trajectory depicted by the dash-dotted line. Markers show trajectories in the vicinity of electric-field antinode according to Eq. (28) with $\lambda_{\parallel+} = \lambda_{\parallel+}^{\mathrm{corr}}$ (triangles) and $\lambda_{\parallel+} = \lambda_{\parallel+}^{\mathrm{Q}}$ (squares). Time along the dotted line in panel (b) is 2.5 times faster.

In the case of large amplitudes $a \gg a_{RR}$, radiation losses change particle motion qualitatively. Figure 4(b) corresponds to the extremely strong field with amplitude $a = 20\,000$. First, particles are trapped by the region of the closest electric-field node. Second, initial conditions can be neglected, which is why there is no stop effect, if radiation reaction is taken into account. The particles rapidly approach the stationary trajectory and then drift slowly to the electric-field node. This is clear from comparison of the dash-dotted curve [radiation reaction (9) is taken into account] and the curve corresponding to Eq. (28) marked by triangles. The good agreement between them confirms correctness of the analytically derived rate of longitudinal drifting. The slowest longitudinal drift is typical for particles that have experienced the greatest radiation losses. Without radiation reaction, the trajectory is approximately the same as that for $a = 100$. In other approaches, the drift is essentially slower in the case of LL (LAD) force or excessively fast in the case of quantum corrections (9). In fact, the use of continuous radiation reaction force is not applicable when the quantum parameter of the particle $\chi \gtrsim 1$. In this case, the particle can lose a substantial part of its energy, and consequently the same part of longitudinal momentum. It needs additional time to be accelerated, to approach the stationary trajectory and to obtain longitudinal momentum. Recently it was noticed on an example of trajectories that, on the average, particles drift longer to the electric-field node in the quasiclassical case than in the case when radiation losses are described as a continuous force [7]. That phenomenon was explained by the straggling effect. The reason of the difference can be clearer from comparison of ponderomotive forces [proportional to $\sin(\varphi)$ as follows from Eq. (3), φ is shown in Fig. 2(b)]. In the quasiclassical case $\sin(\varphi)$ is less than in the case of quantum-corrected force. Thus, the quasiclassical approach gives a more correct result taking into account energy losses and stochasticity of photon emission.

The time spent by the particle to reach the electric-field node t_n as a function of wave amplitude is shown in Fig. 5. Without radiation reaction, t_n is approximately constant $t_n \approx 1.59\mathrm{T}$. Note that t_n differs from t_d. As stated above, the last time interval characterizes the initial stage of drifting in the vicinity of the electric-field node. In a general case, as a result of radiation losses, t_n becomes a monotonically increasing function of a. However, even the classical radiation reaction force with quantum corrections can give an error in calculation of t_n of about 40%. The greater χ, the more probable the emission of a large part of particle energy is and the clearer the stochasticity emerges (compare the solid and dash-dotted curves in Fig. 5). Like in the case of the quantum-corrected RR force, the quasiclassical description shows that, in the vicinity of electric-field antinode, the center of mass is described by $e^{\lambda_{\parallel+}^{\mathrm{Q}}t}$ when $a \gtrsim 860$ and $a \gg a_{RR}$ [Fig. 4(b)], enabling the

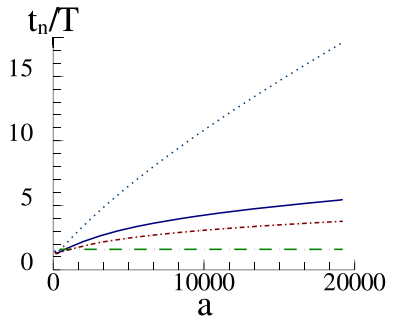

FIG. 5. Time t_n needed for the electron to reach the electric-field node as a function of wave amplitude. The solid line corresponds to the quasiclassical approach. Dotted and dash-dotted lines obtained taking into account radiation reaction force in the form of Landau–Lifshitz and with quantum corrections, respectively. The dashed line represents t_n without radiation losses.

calculation of $\lambda^{Q}_{\parallel+}$ as a function of a through Eq. (28). In this case, for the considered wave amplitudes numerically retrieved $\lambda^{Q}_{\parallel+}$ is shown in Fig. 3(a) and fits

$$\lambda^{Q}_{\parallel+} \approx 4a^{-0.3}. \tag{29}$$

Comparison of $\lambda^{Q}_{\parallel+}$ in the quasiclassical case and in the case with quantum corrected force shows that stochasticity does not change the power law but decreases the factor, $\lambda^{Q}_{\parallel+} \approx 0.73\lambda^{corr}_{\parallel+}$.

Reduction of the rate of longitudinal drifting has a great impact on the development of QED cascades in the field of a circularly polarized standing wave. First, electrons (positrons) spend more time in the vicinity of electric-field antinode and radiate more photons. Second, the longitudinal momentum of photons as well as of electrons is smaller due to radiation reaction, so displacement of the created electron-positron pairs from the electric-field antinode is smaller too.

V. SPATIAL DISTRIBUTION OF e^-e^+ PLASMA

In this section we consider the spatial structures of pair plasmas created in vacuum through QED cascades in a standing circularly polarized wave, especially along the longitudinal direction. We pay particular attention to the avalanche stage, where plasma back reaction can be neglected and therefore field structures are fixed. Although this is the initial stage of QED plasma evolution, these plasma structures may have a strong impact on the subsequent laser-plasma interaction and therefore may be considered as fundamental modes of vacuum breakdown. As QED cascades are generated in the high-field region, we can expect formation in colliding laser pulses of a hump-like density structure in the vicinity of these regions. However, this is not so, in general, because of a very important role of longitudinal particle drifting. In cases of linear and circular polarization, the reasons are qualitatively different. Periodic oscillation of the Poynting vector in the standing linearly polarized wave causes complex periodic dynamics of pair plasma and cascade growth rate. Moreover, the NRT and at higher amplitudes the ART regime suppressing drift to the electric-field node are realized, whereas in a standing wave with circular polarization only the NRT regime occurs, drifting particles to the node region. We will try to give answers to why and when different regimes of pair development occur in the field of a standing circular polarized wave, providing arguments that density distributions may be peaked at the electric-field antinode or node or in both regions.

At the stage of exponential growth of pairs it is natural to assume that hump-like density structures result in the competition of the growth rate of pair production and the corresponding particle escape rate from the high-field region. Moreover, in a standing circularly polarized wave escaping particles are collected in the node region, as is seen in Fig. 1.

Thus, to make estimates we have to compare three parameters. The first parameter is the growth rate of electromagnetic cascade, which is maximal at the antinode where the field structure is a rotating electric field. Development of the cascade in such a field structure has been considered in detail in Refs. [32–34]. The other two parameters are the rate of longitudinal particle drifting to the electric-field node considered above, for which Eq. (29) will be used as a more correct one, and the rate of transverse drifting.

Using the PIC code PICADOR [45] that takes into account quantum effects in the frame of the quasiclassical approach [42] we calculated the cascade growth rate Γ as a function of a in the vicinity of the electric-field antinode. The calculated Γ is accurate to 0.22 with analytical approximation of cascade growth rate in the rotating electric field [33]:

$$\Gamma = 1.33\left(\frac{a}{a_{RR}}\right)^{1/4}\left(\frac{\tilde{\omega}}{\omega_l}\right)^{0.5}\lg\left(\frac{a}{a_{RR}}\right) - 0.22, \tag{30}$$

where $\tilde{\omega} = 2\pi c/10^{-4} = 1.88 \times 10^{15}$ s^{-1} (1 μm wavelength). The threshold amplitude for the cascade development is $a_{cs} \approx 650$, at this amplitude $\chi_{cs} \approx 0.87$.

The transverse drifting implies two effects. First, particles drift in inhomogeneous laser beams, as was considered in Ref. [35]. Following this paper, in the case of weakly inhomogeneous field $E \propto a\exp(-\frac{\mu^2 r^2}{2})$ at $a \gg a_{RR}$ and $\mu \ll 1$ close to the beam axis, the particle escape rate, assuming r (that is of order beam radius $r_b = \sqrt{\ln 2}/\mu$ or less) as a function of time $r \approx r_0\exp(\Gamma_{esc}t)$ is

$$\Gamma_{esc} \approx \frac{5}{8}\mu^2\left(\frac{a_{RR}}{a}\right)^{0.75}. \tag{31}$$

The field amplitude of one beam is $a/2$. This conclusion is valid for large beams with radius $r_b \gtrsim 3\lambda$, which corresponds to $\mu \lesssim 0.1$. For these parameters Γ_{esc} is much less than Γ and $\lambda^{LL}_{\parallel+}$ as well, and transverse drifting can be considered independently and almost does not change the longitudinal drifting. Although this conclusion is analytically proved in the frame of LL (LAD) force, it is also valid for the quantum-corrected force and in the quasiclassical case.

In the case of the LL force, $\Gamma_{esc}/\lambda^{LL}_{\parallel+} = \frac{5\ln(2)}{8r_b^2} = \frac{U}{r_b^2}$ as follows from Eqs. (13) and (23), where $U = 0.43 \sim 1$. In dimensional variables, $\Gamma_{esc}/\lambda^{LL}_{\parallel+} = U/(k_l r_b)^2$ ($k_l = \omega_l/c$) and does not depend on a. These two rates are specified by the ponderomotive force, but in different directions. The characteristic time of escape is proportional to the ratio of the inhomogeneity scale to drift velocity. Moreover, the velocity is proportional to the field gradient, thus inversely proportional to the inhomogeneity scale. The scale is $1/k_l$ in the longitudinal direction, and r_b

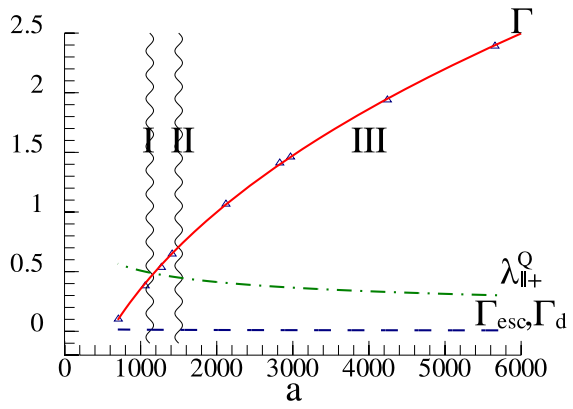

FIG. 6. Dimensionless electromagnetic cascade growth rate Γ (solid line is approximation, triangles are obtained from numerical simulation), rate of longitudinal drift to electric-field node $\lambda_{\|+}^{Q}$ (dash-dotted line), rate of transverse drift Γ_{esc} and transverse diffusion drift Γ_d at the electric-field antinode (dashed line, $\mu \approx 0.1$) versus field amplitude of two colliding circularly polarized laser beams. The dotted wavy lines separate regions of different pair plasma structures shown by Roman numerals.

in the transverse direction. Thereby in any case (LL, LAD, quantum corrected forces, quasiclassical case) we can state that $\Gamma_{esc}/\lambda_{\|+} = U/(k_l r_b)^2$. So, even in a tightly focused field $\Gamma_{esc} < \lambda_{\|+}$. Numerical simulations confirm this conclusion.

Another drifting effect is diffusion due to the stochastic nature of photon emission considered in Sec. III. Its rate is $\Gamma_d = 4d/r_b^2$. When $\chi \gg 1$ from Eqs. (12) and (15) it follows that

$$\Gamma_d \approx \frac{2\eta^{1/3}}{3\alpha r_b^2}\left(\frac{\delta_q}{a}\right)^{(1-s)/3}. \tag{32}$$

In the quantum case $s = 0.25$, $\delta_q \approx 0.37\alpha/\eta^{1/3}$ this gives asymptotically $\Gamma_d/\lambda_{\|+}^{Q} = 0.24/r_b^2$. Diffusion drifting is the order of magnitude of drifting due to field inhomogeneity $\Gamma_d \sim \Gamma_{esc}$ (in the quantum case $\chi \gg 1$) but they are also less important than longitudinal drifting, even for tightly focused laser beams.

In Fig. 6 we summarize all parameters needed for QED cascade development analysis as a function of field amplitude. First of all, we determine the point where

$$\Gamma(a) = \lambda_{\|+}^{Q}(a), \tag{33}$$

i.e., avalanche growth rate is exactly compensated by the particle escape rate. The solution of equation (33), which is

$$a = a_{th1} \approx 1150, \tag{34}$$

defines the threshold of cascade development for the continuous wave, i.e., for e^-e^+ plasma production it should be $a > a_{th1}$. Next, we consider pair production in two regions: antinode and node of the electric field. In the antinode region the pair production rate is $\Gamma(a) - \lambda_{\|+}^{Q}(a)$ and the plasma density as a function of time is $n_a(t) = n_0 e^{(\Gamma-\lambda_{\|+}^{Q})t}$. n_0 is initial plasma density. In the node region the particle growth is $\lambda_{\|+}^{Q}(a)$, because the particles escaping from the antinode drift exactly to the node as shown in Fig. 1. However, the particles need time $\delta t \approx \lambda_{\|+}^{Q\,-1}$ to reach the node region, so $dn_n/dt = \lambda_{\|+}^{Q} n_a(t-\delta t)$, and plasma density in the node region is

$$n_n(t) = \frac{\lambda_{\|+}^{Q}}{\Gamma - \lambda_{\|+}^{Q}} n_0 e^{(\Gamma-\lambda_{\|+}^{Q})(t-\delta t)}. \tag{35}$$

Density peaks in the node and antinode regions are the same, when $n_a(t) \approx n_n(t)$. Consequently,

$$(\Gamma/\lambda_{\|+}^{Q} - 1)e^{\Gamma/\lambda_{\|+}^{Q}-1} \approx 1, \tag{36}$$

having a solution

$$\Gamma \approx 1.57\lambda_{\|+}^{Q}. \tag{37}$$

As follows from Fig. 6, Eq. (37) is satisfied at

$$a = a_{th2} \approx 1500. \tag{38}$$

Thus we can identify three regimes of electromagnetic cascade development. In the case when the intensities just slightly exceed the threshold $0 < \Gamma(a) - \lambda_{\|+}^{Q}(a) \ll \lambda_{\|+}^{Q}(a)$ pairs are located mainly in the vicinity of the node. We mark this regime as regime I in Fig. 6. At the intensities near the second threshold, pairs are located in both antinode and node regions with comparable peak density values (regime II). And regime III occurs at higher intensities $a > a_{th2}$ when the peaks in the node region have a lower density than in the antinode region. In this case, at much higher intensities when $\Gamma(a) \gg \lambda_{\|+}^{Q}(a)$, density distribution will peak around the antinode plane only.

Using the PIC code PICADOR we performed three-dimensional (3D) simulations of cascade development in counterpropagating circularly polarized laser beams with a focus on the avalanche regime, when the plasma back reaction is negligible. The initial plasma seed density n_0 influences only the duration of the avalanche stage, whereas the density distributions normalized to n_0 are the same at this stage for different n_0. To omit the plasma back reaction during simulations we consider the low initial density to be $n_0 = 0.01\ \mathrm{cm}^{-3}$. The initial number of PIC-code macroparticles is 10^5, and one real particle corresponds to 2×10^{23} macroparticles. Laser pulses are half infinite with one wave period leading edge. To eliminate the influence of the leading edge, electrons and positrons appear in numerical simulation in the field region $0.1\lambda_l \times 0.01\lambda_l \times 0.1\lambda_l$ around the point of the maximum of electric-field amplitude when a standing wave is formed. This is reasonable because two counterpropagating circularly polarized laser pulses can strongly compress the plasma target. The simulation box included $224 \times 128 \times 224$ cells and was 3D as $7\lambda_l \times 2\lambda_l \times 7\lambda_l$, the time step was $1/(32\omega_l)$. This grid size and time step are sufficient to simulate laser interaction with transparent plasma with the help of the adaptive event generator utilized in PICADOR [42]. Probabilities of quantum processes are considered in the frame of local constant field approximation, which is justified below QED critical field in the optical range [34,46,47], and the generator can automatically subdivide the time step in order to resolve quantum processes. We performed a parametric scan for a wide range of incident amplitudes. Analysis of the cascade development revealed three different regimes of pair plasma evolution resulting in three types of spatial density structures.

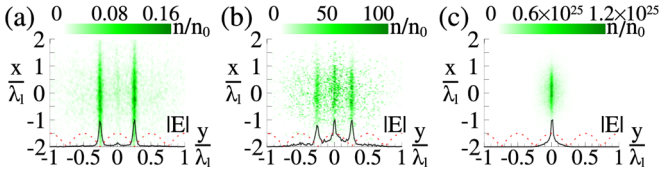

FIG. 7. Pair plasma structures at the initial stage of electromagnetic cascades in the field of two colliding laser beams with $3\lambda_l$ diameter at FWHM and amplitudes (a) $a/2 = 550$, (b) $a/2 = 700$, (c) $a/2 = 2500$. Electron density n is normalized to initial electron density $n_0 = 0.01$ cm^{-3}. The dotted line represents the electric-field magnitude along the symmetry axis of beams $r = 0$. The profile of the electron distribution averaged along the x direction is shown by the solid black line.

As follows from the simulations, the first threshold, when cascades start to develop, is about $a_{\rm th1} \approx 1100$ and the second one, which we defined for the wave amplitude when maximum values of the total pair number over transverse beam section (black solid curves in Fig. 7) are approximately equal, is $a_{\rm th2} \approx 1400$. These threshold values are quite close to those obtained above. According to the numerical simulations, the peaks in the node region disappear when $a > 1900$ and $\Gamma > 2.25\lambda_{\parallel+}^{\rm Q}$. In Fig. 7 we present typical results of 3D simulations for the laser beam radius $r_b = 1.5\lambda_l$ ($\mu \approx 0.1$) in the form of pair plasma distribution after five laser periods for amplitudes $a/2 = 550$, 700, 2500 [Figs. 7(a)–7(c), respectively] . It should be mentioned that there is also transverse drift in the node region. Unlike the antinode region, radiation losses do not suppress transverse drift in the node region, because particle energy is small $\gamma \ll a$ and $F_r \ll 1$. The particles move in the NRT regime there and, as was considered in Sec. II, drift transversely with velocity of about $0.6c$. The corresponding characteristic rate of escape Γ_d^n in dimensionless variables is $0.6/r_b$. For the considered parameters $\Gamma_d^n = 0.064$ is much less than $\lambda_{\parallel+}^{\rm Q}$ and this drift can be neglected. Clearly, the results of simulations are consistent with the three regimes discussed above.

VI. SUMMARY

In this paper we tried to understand what types of fundamental spatial e^-e^+ plasma structures may be realized through QED cascades in counterpropagating laser pulses with circular polarization. To get an insight into the physics, we first presented long-term density distributions, in which asymptotic regimes such as ponderomotive trapping and relativistic chaos are included. It was shown that only the NRT regime is realized taking into account the radiation reaction effect, whereas the ART regime trapping electrons in the vicinity of electric-field antinode does not occur. However, the latter regime is important for linear polarization. Since QED cascades are mainly generated in the high-field region, we presented a general analysis of longitudinal particle drifting at extreme intensities when the quantum radiation reaction effect should be accounted for. For qualitative estimation we also considered the stochastic nature of photon emission, particularly showing that discreteness of emission can additionally decrease drifting rates up to 1.4 times due to strong perturbation of particle motion and generate a new effect of particle diffusion. Based on the comparison of pair production growth rates and the main particle loss rates connected with longitudinal drifting from the electric-field antinode to node we conclude that three fundamental modes of QED cascades may be formed in a standing circularly polarized wave, giving rise to density distributions peaked at antinode or node or in both regions. This conclusion is confirmed by PIC simulations.

ACKNOWLEDGMENTS

The authors acknowledge the support from the Russian Science Foundation Project No. 16-12-10486. The simulations were performed on the resources provided by the Joint Supercomputer Center of RAS. A.V.B. acknowledges support from the Dynasty Foundation.

APPENDIX

For simplicity of numerical calculations it is possible to use the following expression for quantum-corrected RR force, which corresponds to Eq. (9) to an accuracy within 0.15%:

$$F_{ra} \approx \frac{\alpha}{3\sqrt{3}\pi\gamma\eta}\begin{cases} 10.8828\chi^2(1+18.08\chi+68.7\chi^2+70.8\chi^3+7.6403\chi^4)^{-1/3} & \text{if } \chi < 10 \\ -10.8828+6.05498\chi^{2/3}+28.551\chi^{-2/3}-41.469\chi^{-1}+24.7245\chi^{-4/3}-8.1621\chi^{-2} & \text{if } \chi \geqslant 10. \end{cases} \quad \text{(A1)}$$

[1] http://www.eli-beams.eu/.
[2] J. Zou, C. Le Blanc, D. Papadopoulos, G. Cheriaux, P. Georges, G. Mennerat, F. Druon, L. Lecherbourg, A. Pellegrina, P. Ramirez, F. Giambruno, A. Freneaux, F. Leconte, D. Badarau, J. Boudenne, D. Fournet, T. Valloton, J. Paillard, J. Veray, M. Pina, P. Monot, J. Chambaret, P. Martin, F. Mathieu, P. Audebert, and F. Amiranoff, High Power Laser Sci. Eng. **3**, e2 (2015).
[3] A. V. Bashinov, A. A. Gonoskov, A. V. Kim, G. Mourou, and A. M. Sergeev, Eur. Phys. J. Spec. Top. **223**, 1105 (2014).
[4] M. Tamburini, F. Pegoraro, A. D. Piazza, C. Keitel, T. Liseykina, and A. Macchi, Nucl. Instrum. Methods Phys. Res., Sect. A **653**, 181 (2011).
[5] A. Gonoskov, A. Bashinov, I. Gonoskov, C. Harvey, A. Ilderton, A. Kim, M. Marklund, G. Mourou, and A. Sergeev, Phys. Rev. Lett. **113**, 014801 (2014).
[6] L. L. Ji, A. Pukhov, I. Y. Kostyukov, B. F. Shen, and K. Akli, Phys. Rev. Lett. **112**, 145003 (2014).
[7] R. Duclous, J. G. Kirk, and A. R. Bell, Plasma Phys. Control. Fusion **53**, 015009 (2011).

[8] N. Neitz and A. Di Piazza, Phys. Rev. Lett. **111**, 054802 (2013).
[9] S. Yoffe, Y. Kravets, A. Noble, and D. A. Jaroszynski, New J. Phys. **17**, 053025 (2015).
[10] A. V. Bashinov, A. V. Kim, and A. M. Sergeev, Phys. Rev. E **92**, 043105 (2015).
[11] G. Breit and J. A. Wheeler, Phys. Rev. **46**, 1087 (1934).
[12] N. B. Narozhny, A. I. Nikishov, and V. I. Ritus, Sov. Phys. JETP **20**, 622 (1965).
[13] A. R. Bell and J. G. Kirk, Phys. Rev. Lett. **101**, 200403 (2008).
[14] E. N. Nerush, I. Y. Kostyukov, A. M. Fedotov, N. B. Narozhny, N. V. Elkina, and H. Ruhl, Phys. Rev. Lett. **106**, 035001 (2011).
[15] V. F. Bashmakov, E. N. Nerush, I. Y. Kostyukov, A. M. Fedotov, and N. B. Narozhny, Phys. Plasmas **21**, 013105 (2014).
[16] S. S. Bulanov, T. Zh. Esirkepov, A. G. R. Thomas, J. K. Koga, and S. V. Bulanov, Phys. Rev. Lett. **105**, 220407 (2010).
[17] T. Grismayer, M. Vranic, J. L. Martins, R. A. Fonseca, and L. O. Silva, Phys. Plasmas **23**, 056706 (2016).
[18] M. Jirka, O. Klimo, S. V. Bulanov, T. Zh. Esirkepov, E. Gelfer, S. S. Bulanov, S. Weber, and G. Korn, Phys. Rev. E **93**, 023207 (2016).
[19] I. Y. Kostyukov and E. N. Nerush, Phys. Plasmas **23**, 093119 (2016).
[20] W. Luo, Y.-B. Zhu, H.-B. Zhuo, Y.-Y. Ma, Y.-M. Song, Z.-C. Zhu, X.-D. Wang, X.-H. Li, I. C. E. Turcu, and M. Chen, Phys. Plasmas **22**, 063112 (2015).
[21] A. A. Muraviev, S. I. Bastrakov, A. V. Bashinov, A. A. Gonoskov, E. S. Efimenko, A. V. Kim, I. B. Meyerov, and A. M. Sergeev, JETP Lett. **102**, 148 (2015).
[22] M. Vranic, T. Grismayer, R. A. Fonseca, and L. O. Silva, Plasma Phys. Control. Fusion **59**, 014040 (2017).
[23] Z. Gong, R. H. Hu, Y. R. Shou, B. Qiao, C. E. Chen, X. T. He, S. S. Bulanov, T. Zh. Esirkepov, S. V. Bulanov, and X. Q. Yan, Phys. Rev. E **95**, 013210 (2017).
[24] A. Gonoskov, A. Bashinov, S. Bastrakov, E. Efimenko, A. Ilderton, A. Kim, M. Marklund, I. Meyerov, A. Muraviev, and A. Sergeev, arXiv:1610.06404.
[25] G. Lehmann and K. H. Spatschek, Phys. Rev. E **85**, 056412 (2012).
[26] A. D. Steiger and C. H. Woods, Phys. Rev. A **5**, 1467 (1972).
[27] Y. B. Zeldovich, Sov. Phys. Usp. **18**, 79 (1975).
[28] R. Rohrlich, *Classical Charged Particles* (Addison-Wesley, Reading, 1965).
[29] S. V. Bulanov, T. Zh. Esirkepov, J. Koga, and T. Tajima, Plasma Phys. Rep. **30**, 196 (2004).
[30] A. V. Bashinov and A. V. Kim, Phys. Plasmas **20**, 113111 (2013).
[31] P. Zhang, C. P. Ridgers, and A. G. R. Thomas, New J. Phys. **17**, 043051 (2015).
[32] N. V. Elkina, A. M. Fedotov, I. Y. Kostyukov, M. V. Legkov, N. B. Narozhny, E. N. Nerush, and H. Ruhl, Phys. Rev. Spec. Top.–Accel. Beams **14**, 054401 (2011).
[33] E. N. Nerush, V. F. Bashmakov, and I. Y. Kostyukov, Phys. Plasmas **18**, 083107 (2011).
[34] A. M. Fedotov, N. B. Narozhny, G. Mourou, and G. Korn, Phys. Rev. Lett. **105**, 080402 (2010).
[35] A. M. Fedotov, N. V. Elkina, E. G. Gelfer, N. B. Narozhny, and H. Ruhl, Phys. Rev. A **90**, 053847 (2014).
[36] J. G. Kirk, A. R. Bell, and I. Arka, Plasma Phys. Control. Fusion **51**, 085008 (2009).
[37] M. Tamburini, F. Pegoraro, A. D. Piazza, C. H. Keitel, and A. Macchi, New J. Phys. **12**, 123005 (2010).
[38] S. V. Bulanov, T. Zh. Esirkepov, M. Kando, J. K. Koga, and S. S. Bulanov, Phys. Rev. E **84**, 056605 (2011).
[39] V. N. Bayer, V. M. Katkov, and V. S. Fadin, *Radiation of the Relativistic Electrons* (Atomizdat, Moscow, 1973).
[40] A. Nikishov, J. Russ. Laser Res. **6**, 619 (1985).
[41] V. Ritus, J. Russ. Laser Res. **6**, 497 (1985).
[42] A. Gonoskov, S. Bastrakov, E. Efimenko, A. Ilderton, M. Marklund, I. Meyerov, A. Muraviev, A. Sergeev, I. Surmin, and E. Wallin, Phys. Rev. E **92**, 023305 (2015).
[43] T. Zh. Esirkepov, S. S. Bulanov, J. K. Koga, M. Kando, K. Kondo, N. N. Rosanov, G. Korn, and S. V. Bulanov, Phys. Lett. A **379**, 2044 (2015).
[44] L. D. Landau and E. M. Lifshitz, *The Classical Theory of Fields* (Elsevier, Oxford, 1975).
[45] S. Bastrakov, R. Donchenko, A. Gonoskov, E. Efimenko, A. Malyshev, I. Meyerov, and I. Surmin, J. Comput. Sci. **3**, 474 (2012).
[46] N. B. Narozhny, S. S. Bulanov, V. D. Mur, and V. S. Popov, Phys. Lett. A **330**, 1 (2004).
[47] S. S. Bulanov, N. B. Narozhny, V. D. Mur, and V. S. Popov, J. Exp. Theor. Phys. **102**, 9 (2006).